IOP Publishing Superconductor Science and Technology
Supercond. Sci. Technol. 33 (2020) 044015 (17pp) https://doi.org/10.1088/1361-6668/ab7778

Stress, strain and electromechanical analyses of (RE)$Ba_2Cu_3O_x$ conductors using three-dimensional/two-dimensional mixed-dimensional modeling: fabrication, cooling and tensile behavior

Peifeng Gao[1], Wan-Kan Chan[2], Xingzhe Wang[1], Youhe Zhou[1] and Justin Schwartz[3]

[1] Key Laboratory of Mechanics on Western Disaster and Environment, Ministry of Education, College of Civil Engineering and Mechanics, Lanzhou University, Lanzhou 730000, People's Republic of China
[2] Department of Materials Science & Engineering, North Carolina State University, Raleigh, NC, 27695, United States of America
[3] Department of Engineering Science & Mechanics, College of Engineering, The Pennsylvania State University, University Park, PA 16802, United States of America

E-mail: chan.wankan@gmail.com

Received 5 October 2019, revised 23 January 2020
Accepted for publication 18 February 2020
Published 3 March 2020

Abstract

High temperature superconducting (HTS) conductors, represented by Rare Earth-Barium-Copper-Oxide (REBCO) conductors, are promising for high energy and high field superconducting applications. In practical applications, however, the HTS conductors experience different stresses and strains, including residual stresses due to thermal mismatch and tensile stresses due to Lorentz forces, resulting in some circumstances to a reduction in the load-carrying capacity as well as the risk of degradation in conductor critical current. In this study a mixed-dimensional high-aspect-ratio laminated composite finite element model for REBCO conductor is developed for stress and strain analyses in the processes of fabricating and cooling, as well as tensile testing. The model includes all the major constituent layers of a typical REBCO conductor and is experimentally validated. First, the thermal residual stresses and strains accumulated during the fabrication and cooling processes are analyzed by a multi-step modeling method that emulates the manufacturing process. Then, with the residual stresses and strains as initial stresses and strains, the mechanical behavior under a tensile load is studied. Lastly, a phenomenological critical current-strain model based on the Ekin power-law formula and the Weibull distribution function is combined with the mixed-dimensional conductor model to predict the strain dependence behavior of critical current in the reversible and irreversible degradation strain ranges. Simulation results show that the multi-step modeling is an effective method for stress and strain analyses of REBCO conductors during the fabrication and cooling processes and under and tensile loads. Compressive thermal residual stress generated on the REBCO layer during fabrication and cooling strongly affects the subsequent mechanical and current-carrying properties. Stress–strain curves generated by tensile loads are analyzed and experimentally validated at both the conductor and constituent-layer levels. Simulation results for the strain dependence of critical current are in good agreement with experiment data in both the reversible and irreversible degradation stages.

Keywords: REBCO coated conductor, stress/strain and electromechanical analyses, critical current, finite element model, mixed-dimensional modeling method

(Some figures may appear in colour only in the online journal)

List of Nomenclature

Parameter	Description
I_c	Critical current
ε_{irr}	Irreversible strain
$\mathbf{u}$	Displacement vector
$\mathbf{u_i^j}$	Displacement vector of in-contact surface j (superscript) on interface i (subscript)
ε	Strain tensor
$\varepsilon_{\mathbf{el}}$	Elastic strain tensor
$\varepsilon_{\mathbf{th}}$	Thermal strain tensor
$\varepsilon_{\mathbf{pl}}$	Plastic strain tensor
ε_0	Initial strain tensor
T	Temperature
T_{ref}	Reference temperature
$\boldsymbol{\alpha}$	Coefficient of thermal expansion
$\boldsymbol{E}$	Elastic modulus
$\boldsymbol{\upsilon}$	Poisson's ratio
$\mathbf{D}(T)$	Temperature-dependent elasticity matrix
$\boldsymbol{\sigma}$	Stress tensor
$\boldsymbol{\sigma}_0$	Initial stress tensor
$\boldsymbol{\sigma}_\mathbf{y}$	Yield stress tensor
$\mathbf{E_t}(T)$	Temperature-dependent tangent modulus matrix
w_{tape}	Width of the model
l_{tape}	Length of the model
$\mathbf{n}$	Normal vector of the symmetric boundaries
T_1	Initial fabrication temperature, 970 K
T_2	Silver cap layer deposition temperature, 770 K
T_3	Copper electroplating temperature, 330 K
RT	Room temperature, 300 K
$\boldsymbol{\sigma}_{02}$	Initial stress tensor in step S2
ε_{02}	Initial strain tensor in step S2
Ω_{RBH}	Computational domains of the REBCO-buffer-Hastelloy partially-fabricated conductor
Ω_S	Computational domain of silver layer
$\boldsymbol{\sigma}_{03}$	Initial stress tensor in step S3
ε_{03}	Initial strain tensor in step S3
Ω_{SRBH}	Computational domain of the silver-REBCO-buffer-Hastelloy partially-fabricated conductor
Ω_C	Computational domain of copper stabilizer
$\boldsymbol{\sigma}_{0\mathrm{t}}$	Initial stress tensor in tension analyses step
$\varepsilon_{0\mathrm{t}}$	Initial strain tensor in tension analyses step
Ω_{tape}	Computational domain of the fully-fabricated conductor
σ_f^j	In-plane biaxial thermal residual of the jth constituent layer
$E_f^{j'}$	Biaxial modulus of the jth constituent layer
α_f^j	CTE of the jth constituent layer
α_s	CTE of 'substrate' in a laminated composite
k_f^j	Slope of stress-temperature curve of the jth film layer
α_H	CTE of Hastelloy
α_C	CTE of copper
V_H	Volume of Hastelloy layer
V_C	Volume of copper layer
ε_{res}^j	Residual strain of the jth layer
ε_{real}	Real strain
ε_{th}^j	Thermal strain of the jth layer
ΔT	Temperature difference
ε	Applied tensile strain (engineering strain)
σ	Applied tensile stress (engineering stress)
l_0	Original length of the conductor
l	Final length of the conductor
F	Applied force
A_0	Original cross-section area of the conductor
σ_{equ}	Equivalent stress of a composite system
σ^j	Stress of jth constituent layer in the REBCO conductor
V^j	Volume of jth constituent layer in the REBCO conductor
E_{equ-I}	Equivalent conductor-level elastic modulus of the first stage
E_{equ-II}	Equivalent conductor-level elastic modulus of the second stage
σ_{Y-I}	The first conductor-level yield stress
σ_{Y-II}	The second conductor-level yield stress
ε_{in}^s	Internal strain in REBCO layer
σ_{xx}^s	Principal stress of REBCO layer in the longitudinal direction
σ_{yy}^s	Principal stress of REBCO layer in the width direction
σ_{zz}^s	Principal stress of REBCO layer in the thickness direction
E^s	Young's modulus of REBCO

E_t^s	Tangent modulus of REBCO
υ^s	Poison's ration of REBCO
ε_{res}^s	Residual strain on the REBCO layer
σ_V	von-Mises stress
σ_{xx}	Principal stress in the longitudinal direction
σ_{yy}	Principal stress in the width direction
σ_{zz}	Principal stress in the thickness direction
j_ε	Critical current density under strain ε
j_{max}	The maximum critical current density
ε_{max}	So-called maximum strain, at which critical current density becomes a maximum value
j_{c0}	Critical current density under zero-strain
I_ε	Critical current under strain ε
I_{c0}	Critical current under zero-strain
S_{eff}	Effective area of the undamaged cross-section in the REBCO layer under uniaxial deformation
S_0	Cross-section of the REBCO layer under zero-strain
$W(\varepsilon)$	Weibull's distribution function in term of ε
m	Shape parameter of Weibull function
ε_0	Scaling parameter of Weibull function

1. Introduction

The high temperature superconducting (HTS) Rare Earth-Barium-Copper-Oxide (REBCO) conductors are one of the most promising superconducting conductors for high energy, high field applications such as power cables, superconducting magnets and flux pumps for their high critical temperature and high critical current density in the presence of a high background magnetic field [1–7].

REBCO conductors are layered composite materials consisting of multiple laminated high-aspect-ratio (HAR) layers with vastly different material properties; these layers include the stabilizer, silver, REBCO, buffer layers, and the substrate. Due to the differences in coefficients of thermal expansion (CTEs) among the constituent layers, residual stresses and strains accumulate on all the constituent layers when the temperature varies drastically during the heat treatments in the fabrication process and cooling process. Experimental measurements of residual stresses/strains in REBCO conductors reported that high level of compressive residual strain at about −0.2% accumulated on the superconducting film layer when temperature decreased from the initial fabrication temperature to room temperature (RT) [8, 9]. Furthermore, the compressive component of the residual strain induced by the fabrication heat treatments became tensile at the 'force-free strain', at which the internal stress on the REBCO layer changes to zero [8]. Numerical investigations on thermal residual stresses and strains were carried out as well in [10, 11], and their results suggested that residual stresses/strains induced by mismatch of CTEs significantly affected the mechanical and superconducting properties of REBCO conductors.

In practical applications, internal mechanical loads occur among the constituent layers inside a REBCO conductor during and after the conductor and coil fabrication processes and under Lorentz forces during magnet operation. Experimental results and theoretical analyses showed that the critical current (I_c) of a REBCO conductor was influenced by intrinsic strains induced by external forces or deformations [8–25]. The strain effect on I_c can be divided into two regions: reversible and irreversible degradation regions. In the reversible region, the strain-dependent degradation of I_c in a REBCO conductor is gradual and recoverable. One study showed that the reversible strain effect on I_c is because the local critical current density was substantially suppressed by recoverable dislocations at the grain boundaries due to limited deformation on the REBCO layer [12]. Moreover, first-principles calculations showed that the strain effect on superconducting properties was also influenced by a deformation-induced charge redistribution, which lead to a self-doping process of hole-transfers between CuO_2 plane and Cu–O chain in the cuprate superconductors [13]. In the irreversible degradation region, when a deformation exceeds a certain critical strain value (i.e. the irreversible strain, ε_{irr}), I_c degrades dramatically and irreversibly [8, 9, 11–17]. For example, experimental data showed that I_c of a typical REBCO conductor started to decline rapidly at around 0.7% tensile strain and the normalized I_c degraded 50% at a tensile strain of about 0.8% [8]. Scanning electron microscopy (SEM) showed that transverse crack arrays were generated in yielded samples [18] and edge and 'shattered' cracks were detected in the REBCO layers when severe I_c reduction occurred [19]. Furthermore, micro-cracks in the REBCO layer were detected through magneto-optical (MO) images for applied strains larger than ε_{irr} [17]. The dramatic degradation of I_c in REBCO conductor was suggested to be attributed to the initiation of cracking and damage evolution on the REBCO film. Furthermore, as a laminated layered composite, the stress and strain states in the REBCO superconducting layer within the conductor are influenced by the adjacent layers, such as the substrate and stabilizer.

It is therefore important to understand the evolution of the stress and strain distributions in all the constituent layers of a REBCO conductor under different construction and operational conditions when designing a superconducting magnet with high reliability and sustainable structural integrity. However, it remains difficult to experimentally observe static details, let alone *in situ* dynamic details, of the stress and strain distributions on each constituent layer within a conductor. A computational approach is the most viable and effective way to study the evolution of the sublayer-level stress and strain distributions within a REBCO conductor and their influences on I_c in different processes such as fabrication, cooling and tensile loading.

As typical REBCO conductors contain multiple laminated HAR thin layers, effective modeling is a significant

challenge. This is mainly because the number of non-degenerated finite elements required to approximate geometrically with sufficient accuracy a composite that contains HAR thin layers would be enormously large. Direct meshing of the thin layers and scaling to reduce the aspect ratio [10, 11, 20–23] are some common practices in treating thin layers computationally. Prior finite element (FE) analyses of stress distributions on the constituent layers of a REBCO conductor during fabrication and cooling processes and under external mechanical load [10, 11, 20–23] did not include all the major constituent thin film layers. For example, it is common that the REBCO and buffer layers are considered as a single layer to reduce the difficulty of modeling separately the laminated thin films [21–23]. Theoretical and numerical results, however, indicated that the properties of buffer layer strongly affected the properties of the superconducting layer [24, 25]. Homogenizing or simplifying the two components as one layer representing the superconducting layer misses the influential effects caused by the buffer layer and lead to inaccurate simulation results.

Here a three-dimensional/two-dimensional (3D/2D) mixed-dimensional FE structural model for REBCO conductors is developed for detailed stress and strain analyses. The 3D/2D mixed-dimensional modeling techniques, which has been successfully applied to quench and delamination simulations of REBCO conductors [26–28], is an efficient and effective approach to overcome the meshing and computational problems associated with modeling HAR laminated thin film layers in FE model. The key technique of the mixed-dimensional approach is to model the laminated HAR thin film layers, namely, the silver, REBCO and buffer layers, as separated 2D laminated surfaces, independent of the thickness of each layer. The conductor model includes all the major constituent layers and is experimentally validated. Stress and strain analyses are performed under conditions occurring during fabrication, cooling and tensile loading. First, the thermal residual stresses and strains accumulated during the fabrication and cooling processes are analyzed. Then with the residual stresses and strains acting as initial conditions, the mechanical behavior under tension loads is studied. Finally, a phenomenological model for the strain dependence of I_c under uniaxial tensile load is presented by combining the FE model with the Ekin power-law formula [29] and the Weibull statistic distribution function [30]. The Ekin power-law formula and Weibull distribution function have been used to predict respectively the reversible and irreversible strain-dependence properties of I_c in REBCO conductors [8, 12, 31, 32]. The simulation results for the tensile test and I_c versus strain are shown to be in good agreement with experimental data.

2. Numerical modeling

2.1. 3D/2D mixed-dimensional model

The 3D/2D mixed-dimensional structural model for REBCO conductor is implemented in FE using COMSOL Multiphysics. The model is based on Superpower's REBCO conductor [33] and includes all the main conductor layers, including the stabilizer, substrate, and the laminated thin films, including the silver, REBCO, and buffer layers, as shown in figure 1.

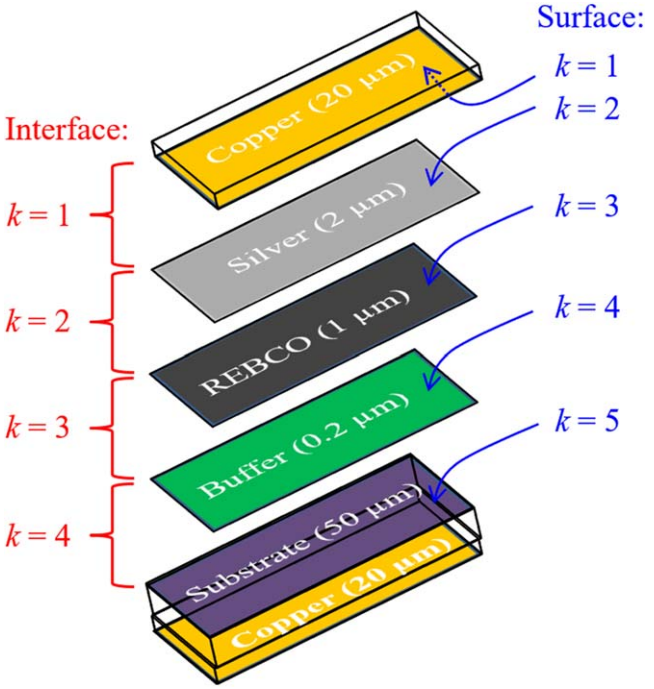

Figure 1. A representative implementation of a 3D/2D REBCO conductor model. Thicknesses (not to scale) of the physical layers and names of the surfaces and interfaces are shown.

Similar to [26–30], the HAR thin film layers are modeled as 2D surfaces while the relatively thick stabilizer and substrate are implemented in 3D domains. This mixed-dimensional modeling approach overcomes the difficulties in modeling 3D HAR thin layers in mesh-based numerical methods such as FE and makes computation much more efficient, which has been demonstrated in [26–28].

The implementation techniques of the mixed-dimensional structural model is similar to those of the delamination model presented in [28], except they are tailored for stress and strain analyses in fabrication, cooling and tensile loading procedures. The main difference is that instead of a spring-based interface constitutive equation, a displacement continuity constraint is defined on each interface to connect rigidly the two in-contact surfaces that the interface lies between. Referring to figure 1, the continuity constraint on interface k ($k = 1, \ldots, 4$) located between two in-contact surfaces k and $k + 1$ ($k = 1, \ldots, 4$) is:

$$\mathbf{u}_{\mathbf{k}}^{\mathbf{k}} = \mathbf{u}_{\mathbf{k}}^{\mathbf{k}+1}, \tag{1}$$

where $\mathbf{u}_{\mathbf{i}}^{\mathbf{j}}$ represents the displacement vector of in-contact surface j (superscript) on interface i (subscript). This constraint ensures that the displacements on two in-contact surfaces k and $k + 1$ at the same material coordinate are always equal, regardless of deformation. This implies that the two in-contact surfaces are in perfect, non-slip, non-tear binding.

Refer to [28] for details about how laminated 2D surfaces are implemented in COMSOL.

Besides perfect binding, it is also assumed that the temperature variation at any time in the fabrication and cooling processes is slow enough that uniform temperature is always established in the entire conductor. Isotropic elasto-plastic mechanical properties are also assumed on all constituent layers.

Under the above assumptions, the strain tensor ε for a small deformation is given as:

$$\varepsilon = \frac{1}{2}[(\nabla \mathbf{u})^{\mathrm{T}} + \nabla \mathbf{u}]. \tag{2}$$

In general, the strain in equation (2) consists of elastic, thermal, initial, and plastic contributions, that is:

$$\varepsilon = \varepsilon_{\mathbf{el}} + \varepsilon_{\mathbf{th}} + \varepsilon_0 + \varepsilon_{\mathbf{pl}}, \tag{3}$$

where $\varepsilon_{\mathbf{el}}$ is the elastic strain tensor, $\varepsilon_{\mathbf{th}}$ is the thermal strain tensor, ε_0 is the initial strain tensor and $\varepsilon_{\mathbf{pl}}$ is the plastic strain tensor. The thermal strain tensor, $\varepsilon_{\mathbf{th}}$, is calculated as:

$$\varepsilon_{\mathbf{th}} = \int_{T_{ref}}^{T} \boldsymbol{\alpha} dT, \tag{4}$$

where T is the temperature, T_{ref} is the reference temperature and $\boldsymbol{\alpha}$ is the coefficient of thermal expansion.

For a linear elastic deformation condition, there is no plastic deformation; the constitutive model is described as:

$$\boldsymbol{\sigma} = \mathbf{D}(T)(\varepsilon - \varepsilon_{\mathbf{th}} - \varepsilon_{\mathbf{0}}) + \boldsymbol{\sigma}_{\mathbf{0}}, \tag{5}$$

where $\mathbf{D}(T)$ is the temperature-dependent elasticity matrix, which is derived from the elastic modulus $\mathbf{E}$ and Poisson's ratio υ of the materials [34], $\boldsymbol{\sigma}$ is the stress tensor and $\boldsymbol{\sigma}_0$ is the initial stress tensor.

Silver, copper and Hastelloy in REBCO conductor are typical ductile materials, and so they can generally become hardened or softened after yielding. In this paper, von-Mises yield criterion and bilinear kinematic hardening properties are adopted to describe the strain-hardening behavior. The constitutive model for a plastic deformation condition is described as:

$$\boldsymbol{\sigma} = \boldsymbol{\sigma}_{\mathbf{y}} + \mathbf{E}_{\mathbf{t}}(T)\varepsilon_{\mathbf{pl}}, \tag{6}$$

where $\boldsymbol{\sigma}_{\mathbf{y}}$ is the yield stress tensor, and $\mathbf{E}_{\mathbf{t}}(T)$ is the temperature-dependent tangent modulus matrix. A tangent modulus defines the stress–strain slope of strain-hardening/softening after yielding. Although REBCO and buffer layers are brittle ceramic materials, the failure of which is fracture, plastic deformation constitutive model is also used for the brittle ceramic layers. An occurrence of a damage on a brittle material, for example, in the form of cracking, causes some relaxation changes in stresses and strains that appear to be due to some sort of yield-like softening behavior [8, 35]. Based upon this fact, the model uses an onset of plastic deformation at yield point on a brittle layer as the criterion to determine an occurrence of damage on that layer. Capturing the stresses and strains at the onset of damage, i.e. at the yield point in modeling, of the REBCO and buffer layers is critical for an electromechanical analysis. In particular, on the REBCO layer, such yielding condition represents the onset of an irreversible degradation of I_c. The stress/strain behavior on the REBCO and buffer layers after the occurrence of the initial damage, i.e. after the yielding in simulation, has little effects on the electromechanical and overall mechanical behavior of the conductor. This is because the thicknesses of the REBCO and buffer layers are very thin relative to the thickness of the conductor; thus, the overall mechanical properties of the conductor are hardly affected by the mechanical behavior on the REBCO and buffer layers. In other words, the adoptions of either a linear or plastic material constitutive models on the brittle layers are immaterial [10, 11] to the after-yield behavior of the conductor.

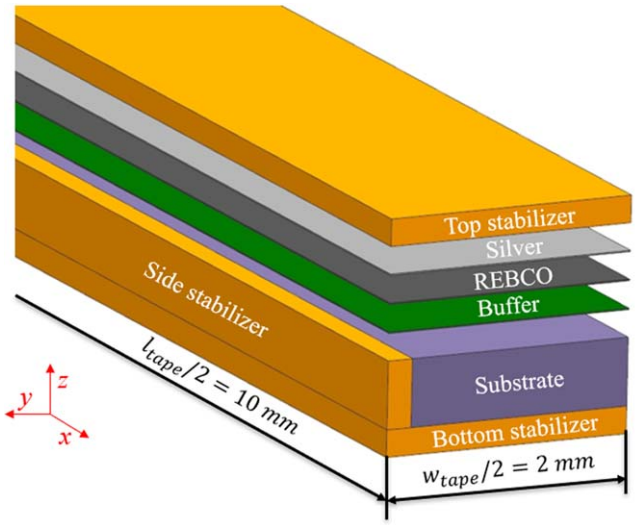

Figure 2. Schematic diagram of a quarter of the conductor model (not to scale).

2.2. Model geometry and materials properties

The conductor model, which is based on SuperPower's SCS4050 conductor [33], has a dimension of width $w_{tape} = 4$ mm and length $l_{tape} = 20$ mm. The thicknesses of all the constituent layers are modeled in real dimensions, as shown in figure 1. Due to the spatial symmetry of the structure and boundary conditions, only a quarter of the conductor is modeled, as shown in figure 2, which shows that a 20 μm thick copper stabilizer also surrounds the sides of the conductor. The symmetric boundaries satisfy $\mathbf{n} \cdot \mathbf{u} = 0$, in which $\mathbf{n}$ is the normal vector on the symmetric boundaries, and $\mathbf{u}$ is displacement vector. To simplify simulation, the conductor is always laid flat by setting the constraint $\mathbf{u} = \mathbf{0}$ on the bottom surface of the substrate.

Table 1 lists the material parameters for all the constituent materials; most are adopted from multiple sources [8, 10, 11, 17, 25, 36–38]. Only the Young's moduli, yield strengths and tangent moduli of copper and Hastelloy are temperature-dependent and they are obtained from parameter fitting on the experimental data reported in [17]. As the buffer layer in a typical IBAD-based superconductor consists of

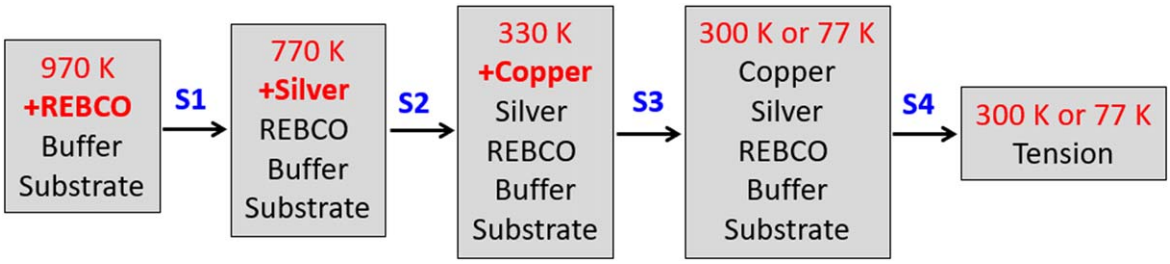

Figure 3. Modeling steps for fabrication and cooling processes and subsequent tensile loading of a REBCO conductor.

several thin layers [25], its Young's modulus, Poisson's ratio and CTE are estimated by volume-weighted-average calculations based on the experimental data reported in [25]. The CTE of Hastelloy is chosen as 14, which is in the range between 10.9 and 16 reported in [8, 10, 11, 25, 38]. The REBCO yield strength is obtained from parameter fitting on the experimental data in [8]. No data is available for the yield strength of the buffer, but because of the likely weak mechanical effects of the buffer layer due to its extreme thinness (0.2 μm), it is modeled as being the same as REBCO. There is also no data available for the tangent moduli of REBCO and buffer. Recall that a tangent modulus defines the behavior of strain-hardening/softening after yielding and the latter when applied to a brittle layer is considered as the onset of irreversible damage. It is likely that the mechanical behavior of a broken thin brittle material has little mechanical effects on other components in a layered composite. Therefore, the tangent moduli of the two brittle thin layers are chosen as a small value of 1 GPa, which adds insignificant mechanical effects but allows better computational convergence. In fact, simulations show that due to the thin thicknesses of the REBCO and buffer layers, changing the values of their moduli has little effect on the overall stress and strain simulation results.

2.3. Analysis details

The stress and strain analyses of REBCO conductors presented here are performed for the fabrication and cooling processes and subsequently under tensile loading. The sequence of the simulation steps is illustrated schematically in figure 3. The entire simulation sequence is designed according to conductor and coil fabrication procedures reported in the literature [8, 11, 25, 39] and are simplified into four main steps. Step S1: starting from the MOCVD process that creates the REBCO film on the buffer-substrate partially-fabricated conductor at an intermediate fabrication temperature of 970 K, the fabrication temperature changes from 970 K (T_1) to 770 K (T_2). Step S2: Silver cap layer is deposited on the REBCO film at 770 K and the temperature is then changed from 770 to 330 K (T_3). Step S3: The copper is electroplated around the conductor to create the surround copper stabilizer at 330 K. The fabrication process is now completed. The temperature is then cooled from 330 K to RT or 77 K. Step S4: Tension load is applied on the fully-fabricated conductor at RT or 77 K with the thermal residual stresses/strains accumulated from all the prior fabrication steps acting as initial stresses/strains. During the fabrication and cooling processes, i.e. from step S1 to step S3, only the temperature load but no external mechanical load is applied and mechanical free boundary conditions are applied on all the non-symmetric boundaries. In the last step the tensile load is applied as a displacement boundary condition in the longitudinal direction on one end of the conductor to create a strain from 0% to 2%.

In the fabrication process analysis, new constituent layers are added one by one to the model using the following multi-step approach. Step 1: A complete conductor model, with all layers included, is built with the same ends of all layers constrained to the same 'locked' displacement. Step 2: Very 'soft' mechanical material properties, e.g. Young's moduli with very small values, are applied to layers that are yet to be added so that they extend or contract easily without adding much stresses to the 'partially-fabricated' conductor. The 'locked' displacement constraints ensure that all the layers have the same length at the end of one fabrication step. Step 3: When a 'new' layer is added, its mechanical material properties are changed back to their normal values. Step 4: The residual stresses and strains from the previous step, i.e. from all the 'added' layers, are input as the initial stresses and strains for the next step.

Before the silver cap layer is added to the REBCO layer, thermal residual stresses and strains have accumulated on the REBCO, buffer, and substrate layers in step S1 when the temperature varies from T_1 to T_2. These residual stresses and strains are defined as the initial stresses and strains on the REBCO-buffer-substrate partial-conductor as:

$$\begin{cases} \boldsymbol{\sigma}_{02} = \boldsymbol{\sigma}|_{T=T_2} \\ \varepsilon_{02} = \varepsilon|_{T=T_2} \end{cases} \text{ in } \Omega_{RBH}, \tag{7a}$$

while the initial stresses and strains on the silver layer are set to zero, i.e.:

$$\begin{cases} \boldsymbol{\sigma}_{02} = 0 \\ \varepsilon_{02} = 0 \end{cases} \text{ in } \Omega_S, \tag{7b}$$

where $\boldsymbol{\sigma}_{02}$, ε_{02} are respectively the initial stress and strain tensors in step S2 analysis, Ω_{RBH} represents the computational domains of the REBCO-buffer-Hastelloy partial-conductor, and Ω_S is the computational domain of the silver layer. Note that the silver layer is not involved in the calculation in

Table 1. Material properties of all the constituent materials of the REBCO conductor [8, 10, 11, 17, 25, 36–38].

	Young's modulus E (GPa)		Poisson's ratio υ	Yield strength σ_y (MPa)		Tangent modulus E_t (GPa)	CTE α ($\times 10^{-6}$ K^{-1})
Temperature (K)	77	300		77	300		
Copper	85	70	0.34	330	190	5	17.7
	[17]	[17]	[11]	[17]	[17]	[17]	[8, 10, 11]
Silver	76		0.37	14		1	17.1
	[36, 37]		[36]	[36, 37]		[36]	[10, 36]
REBCO	157		0.3	1030		1	11
	[8, 10, 11, 25, 38]		[10, 11]	[8]			[8, 10, 11]
Buffer	170		0.226	1030		1	9.5
	[25]		[25]				[25]
Hastelloy	178	170	0.307	1200	980	6	14
	[17]	[17]	[11]	[17]	[17]	[17]	[8, 10, 11, 25, 38]

step S1 and for this reason, the initial stresses and strains on the silver layer for step S2 are set to zero.

Similarly, the initial stresses and strains in step S3 are defined as:

$$\begin{cases} \boldsymbol{\sigma}_{03} = \boldsymbol{\sigma}|_{T=T_3} \\ \varepsilon_{03} = \varepsilon|_{T=T_3} \end{cases} \text{in } \Omega_{SRBH}, \tag{8a}$$

$$\begin{cases} \boldsymbol{\sigma}_{03} = 0 \\ \varepsilon_{03} = 0 \end{cases} \text{in } \Omega_C, \tag{8b}$$

where $\boldsymbol{\sigma}_{03}$, ε_{03} are respectively the initial stress and strain tensors, Ω_{SRBH} represents the computational domains of the silver-REBCO-buffer-Hastelloy partial conductor, and Ω_C is the computational domain of copper stabilizer. Note that the copper stabilizer is not involved in the calculation in step S2 and for this reason, the initial stresses and strains on the copper stabilizer for step S3 are set to zero.

In the tensile load analysis, the stresses and strains accumulated from step S1 to step S3 are defined as the initial stresses and strains on the fully fabricated conductor in step S4 as:

$$\begin{cases} \boldsymbol{\sigma}_{0t} = \boldsymbol{\sigma}|_{T=\text{RT or 77 K}} \\ \varepsilon_{0t} = \varepsilon|_{T=\text{RT or 77 K}} \end{cases} \text{in } \Omega_{tape}, \tag{9}$$

where $\boldsymbol{\sigma}_{0t}$, ε_{0t} are respectively the initial stress and strain tensors in the tensile loading step (step S4), respectively. Ω_{tape} represents the computational domain of the fully-fabricated conductor, which now includes the copper stabilizer, silver, REBCO and buffer layers, and Hastelloy substrate.

3. Results and discussion

As isotropic, elastoplastic material properties are used for all constituent layers in the model and the stresses induced by thermal mismatch are mainly in-plane biaxial stresses (nearly zero in the thickness direction) on all conductor layers, about the same thermal residual stresses are generated in both the longitudinal and width directions on each layer. When a REBCO conductor-based coil operates under normal working condition, Lorentz forces typically generate stresses much larger in the longitudinal direction than in the width direction. This situation holds when winding tension is applied during coil fabrication and when the coil is cooled to cryogenic temperature. The aim of this work is to study the mechanical behavior and its effect on the critical current under the residual stresses due to thermal mismatch and tension that arise during fabrication, cooling, and tensile loading. Therefore, here the analyses focus on the stress and strain properties in the longitudinal direction. Hereafter, unless stated otherwise, 'stress' and 'strain' respectively refer to the stress and strain components in the longitudinal direction. In addition, based on the analysis in the appendix, the stress distribution on each layer is almost homogeneous across the width direction of the conductor; a slight variation in stress distribution only appears on a narrow region along each edge of the conductor. A similar situation occurs with the strain distribution on each layer. As a result, point-value stress and strain distributions on each constituent layer are measured at the layer's center (in width and thickness (for 3D domains) directions), which is within the homogeneous stress and strain distribution region. Also note that the stresses and strains on the top and bottom copper are approximately the same and thus only the stress and strain information on the top copper layer is presented.

3.1. Fabrication and cooling processes simulations

3.1.1. Residual stress distributions on all constitute layers.

Figure 4 shows the changes in the thermal residual stresses in the longitudinal direction on all constituent conductor layers as the temperature varies from 970 to 77 K during the fabrication and cooling processes. The residual stresses and strains on the partially-fabricated buffer-substrate conductor at the beginning of the studied fabrication process are assumed zero at the initial temperature 970 K. Note that the thermal residual stresses on the REBCO and buffer layers are always negative, indicating that these two layers experience only compressive stresses during fabrication and cooling. This is due to the fact that the CTEs of REBCO and buffer are smaller than those of the other components (see table 1). In addition, as the CTE of buffer is smaller than that of REBCO, the residual compressive stress in the buffer layer is always

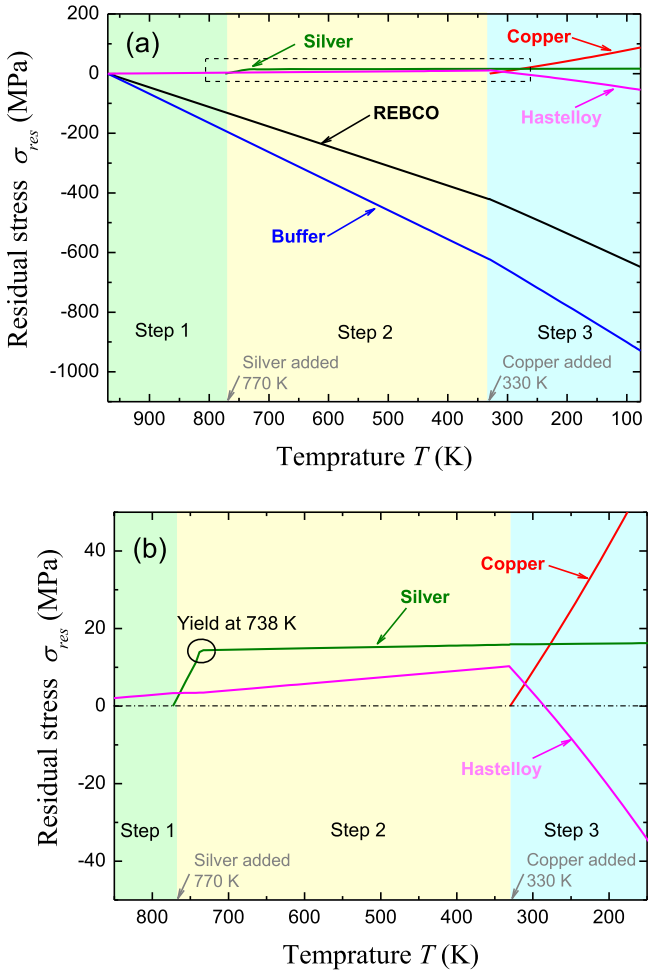

Figure 4. (a) Thermal residual stresses on all the constituent layers versus temperature during fabrication and cooling processes. (b) Details for the dotted-line frame in (a).

larger than that in the REBCO layer. The compressive stresses on these two layers increase linearly as a function of temperature and the slope increase for $T \geqslant 330$ K after the copper stabilizer, which has the largest CTE, is electroplated around the conductor. The in-plane biaxial thermal residual stress distributions in a thin film layer of laminated composites can be expressed [25] as:

$$\sigma_f^j = E_f^{j'}(\alpha_s - \alpha_f^j)\Delta T, \tag{10}$$

where σ_f^j, $E_f^{j'}$ and α_f^j represent the in-plane biaxial thermal residual stress, the biaxial modulus and the CTE of the jth thin constituent layer (here $j = 1, \ldots, 3$ refers to the silver, REBCO and buffer, respectively), α_s is the equivalent CTE of the thick 'substrate', and ΔT is the temperature change. Here 'substrate' represents a partially or fully fabricated composite that includes all the relatively thick layers, namely the Hastelloy substrate and/or the copper stabilizer but excludes all the thin films. The thin films are omitted from the substrate because their contributions to the stress calculation of the jth layer are negligible due to their diminutive thicknesses. The slope of stress-temperature curve of the jth film layer is:

$$k_f^j = \frac{\sigma_f^j}{\Delta T} = E_f^{j'}(\alpha_s - \alpha_f^j). \tag{11}$$

Before the copper stabilizer is added, the 'substrate' is simplified as only the Hastelloy layer, so $\alpha_s = \alpha_H$, where α_H is the CTE of Hastelloy. After the copper stabilizer is added, the 'substrate' is treated to contain both the copper and Hastelloy layers, and the equivalent CTE of the 'substrate' is estimated by volume-weighted-average as:

$$\alpha_s = \frac{\alpha_C V_C + \alpha_H V_H}{V_C + V_H}, \tag{12}$$

where α_C is the CTE of copper, V_C and V_H are the volumes of the copper and Hastelloy layers. Since $\alpha_C > \alpha_H$ (17.7 versus 14), the value of α_s in equation (11) must be larger than α_H, while E_{fi}' is invariant. As a result, the slopes of the residual stress-temperature curves of the REBCO and buffer layers become larger when $T \geqslant 330$ K. In contrast, there is no obvious change in the slopes of the curves at 770 K when the silver layer is deposited on the REBCO layer although the CTE of silver (17.1) is also greater than those of the REBCO and buffer layers. This is simply because the silver layer thickness is small and its Young's modulus (76 GPa) is also relatively small compared to the ceramic REBCO and buffer layers; as a result, the influence of the silver on the REBCO and buffer layer is negligible.

The magnitudes of the thermal residual stresses on other layers are much smaller than those on the REBCO and buffer layers, but some important information is revealed in the inset for the dotted-line frame in figure 4(a). In the inset figure 4(b), the silver layer yields early at $T = 738$ K due to its small yield strength. In addition, before the copper layer is added, the thermal residual stress on the Hastelloy substrate is tensile and increases with decreasing temperature. After the copper layer is added, however, the stress on the Hastelloy eventually becomes compressive as temperature decreases. The CTE of the Hastelloy substrate alone is slightly smaller than the combined CTE of the three thin films, causing the stress on the substrate to become tensile before copper is added. The copper layer has a total thickness comparable to that of the Hastelloy and a CTE larger than that of the Hastelloy, so the presence of the copper layer results in compressive stress in the Hastelloy with decreasing temperature. Thus, when cooling is completed, the thermal residual stresses on the buffer, REBCO, and Hastelloy layers are compressive, while those on the silver and copper layers are tensile.

Figure 5 shows the residual stress distributions due to thermal mismatch on all the constituent layers at RT (solid line) and 77 K (dashed line). Due to their smaller CTEs and thinner thicknesses, the REBCO and buffer layers experience much larger compressive stresses than the other layers: −446 MPa at RT and −648 MPa at 77 K on the REBCO layer and −658 MPa at RT and −929 MPa at 77 K on the buffer layer. The silver layer, which has the second largest CTE and the smallest yield strength resulting in early yielding at $T = 738$ K, as shown in figure 4, experiences much smaller

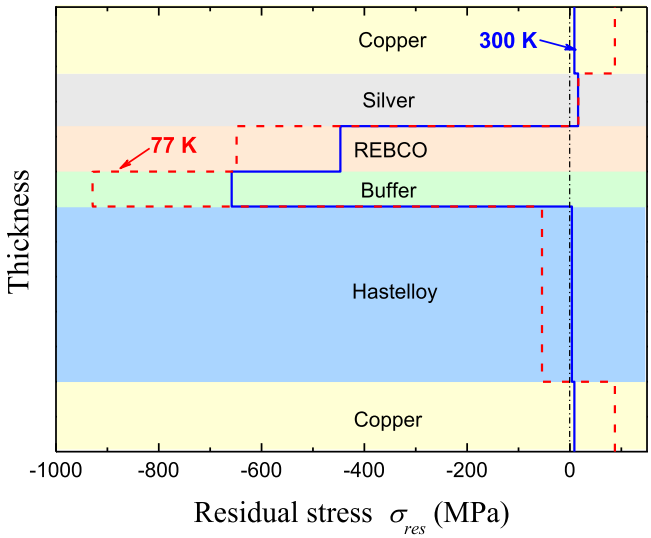

Figure 5. Thermal residual stress distributions on all constituent layers at RT (solid) and 77 K (dashed). Thicknesses are not to scale.

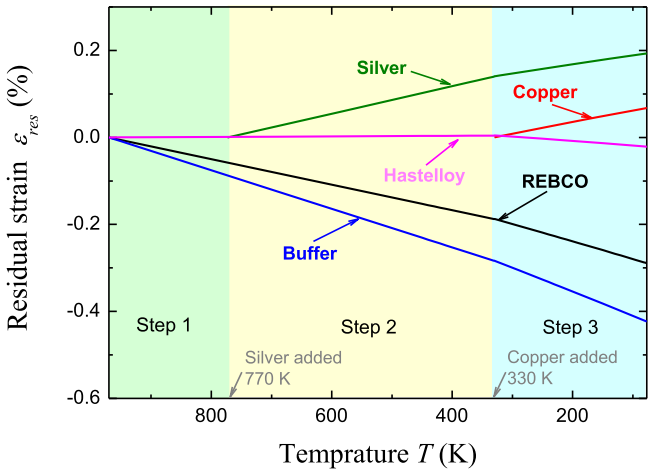

Figure 6. Thermal residual strains on all the constituent layers versus temperature during fabrication and cooling processes.

tensile stress, only about 16 MPa, even at 77 K. The stress on the copper stabilizer, with the largest CTE, is 9 MPa at RT and 88 MPa at 77 K. The stress on the Hastelloy substrate changes from only 4 MPa at RT to −54 MPa when cooled to 77 K. Since copper is added at 330 K, the temperature variation on the stabilizer at RT is only 30 K, therefore, it has little effect on the stress distributions on the substrate and other layers at RT. At 77 K, however, the large contraction of the stabilizer leads to compressive stress distribution on the substrate and increased compressive stresses on the REBCO and silver layers.

Note that all the thermal residual stresses on the constituent layers shown above are intrinsic stresses internal to the conductor. Thus, a conductor that is mechanically free from any constraint and external force should have null total residual stress at any temperature. When observed at the composite conductor level, the equivalent stress of the composite can be expressed by the volume-weighted-average:

$$\sigma_{equ} = \frac{\sum \sigma^j V^j}{\sum V^j}, \tag{13}$$

where σ^j and V^j represent the stress and volume of the jth constituent layer (j refers to copper, silver, REBCO, buffer or Hastelloy), respectively. The equivalent stresses of the conductor at RT and 77 K calculated by (13) using the residual stress values shown in figure 5 are close to zero at 0.098 MPa and 0.123 MPa, respectively. The small nonzero equivalent stresses are attributed to the facts that in simulations the effects of the side stabilizer and inhomogeneous stress distributions appearing near the edges on all the constituent layers (see the appendix) are neglected and the conductor is always constrained to lay flat.

3.1.2. Residual strain distributions on all constitute layers at RT and 77 K. The residual strain ε^j_{res} of the jth layer (j refers to copper, silver, REBCO, buffer or Hastelloy) generated from thermal mismatch can be obtained as:

$$\varepsilon^j_{res} = \varepsilon_{real} - \varepsilon^j_{th}, \tag{14}$$

where ε_{real} is the real strain of the REBCO conductor composite as a whole and is obtained from the fabrication and cooling simulations by imposing the same edge/boundary constraints and temperature difference on all the constituent layers. According to (14), the changes in the thermal residual strains on all the constituent layers as temperature varies from 970 to 77 K during fabrication and cooling are shown in figure 6. The strain curves, except that on the silver layer, vary in trends similar to those of the corresponding stress curves shown in figure 4; this is because each remains in the elastic region. On the silver layer, however, even though its residual stress does not change much after it yields at $T = 738$ K, the residual strain continues to increase with decreasing temperature, even after yielding. The strain in the silver includes the contribution from plastic deformation after yielding. After the copper is added, the slope of the strain—temperature curve decreases because the copper layer has a slightly larger thermal contraction than the silver layer. At the end of the fabrication and cooling processes, the tensile residual strains on the silver layer are larger than those of the copper stabilizer, albeit the tensile residual stresses on the silver layer are smaller than those on the copper stabilizer.

To validate the necessity of the multi-step, layer-by-layer fabrication modeling method outlined in section 2.3 for finding the residual stresses/strains, a one-step fabrication test model is used to generate comparison results. The one-step model computes the stress and strain evolutions in one single fabrication step, i.e. starting with all the constituent layers of the conductor included with actual material properties at the initial fabrication temperature 970 K. Figure 7 shows the comparison of thermal residual strains on the REBCO layer versus temperature during the fabrication and cooling processes between the two modeling methods. As the CTE of copper is larger than REBCO, the accumulated compressive residual stress and strain calculated from 970 to 77 K by the one-step method is much larger than that by the multi-step

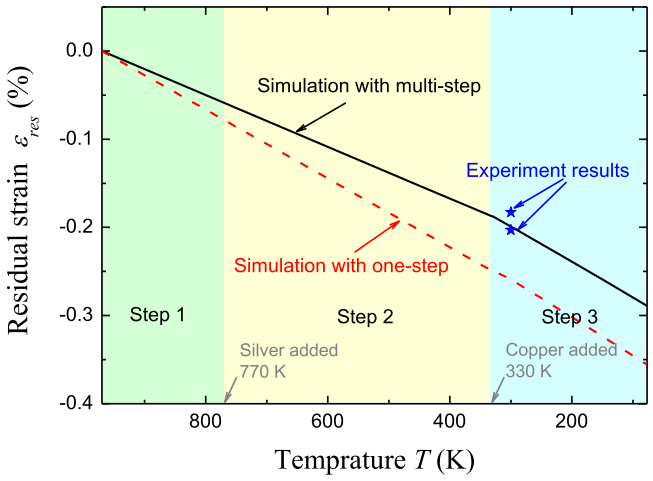

Figure 7. Comparison of thermal residual strains on the REBCO layer versus temperature during the fabrication and cooling processes between the multi-step and one-step modeling methods.

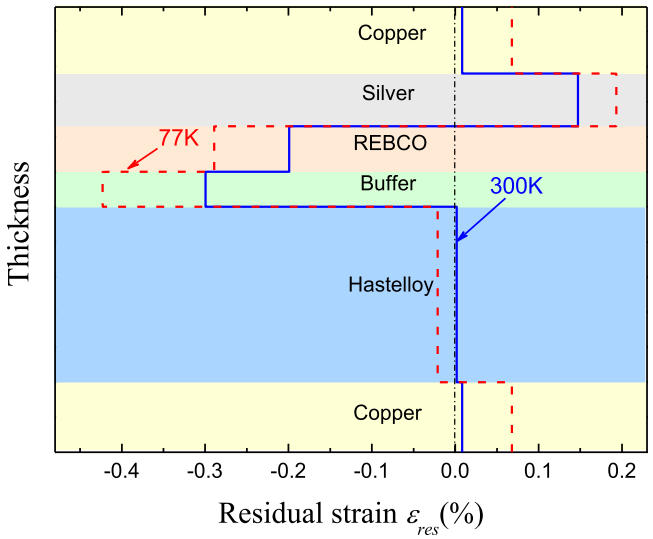

Figure 8. Thermal residual strain distributions in all the constituent layers at RT (solid) and 77 K (dashed). Thicknesses are not to scale.

Table 2. The summary of the residual strain in the REBCO layer at RT and 77 K.

	Residual strain in the REBCO layer (%)	
	RT	77 K
Experiment [8]	−0.20	—
Analytical [8]	−0.17	−0.26
FE modeling [11]	−0.17	−0.24
Multi-step simulation	−0.20	−0.28

method. This indicates that it is necessary to use the multi-step modeling method to obtain good accuracy in mechanical properties of a REBCO conductor during the fabrication and cooling processes.

Table 2 summaries the residual strains on the REBCO layer at RT and 77 K, which are taken from the experimental

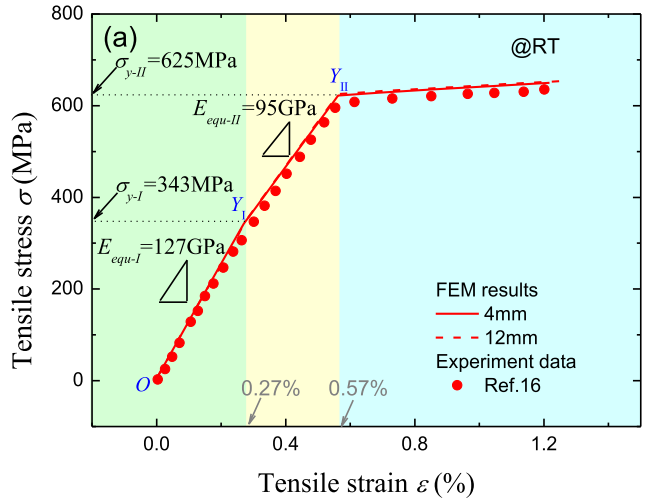

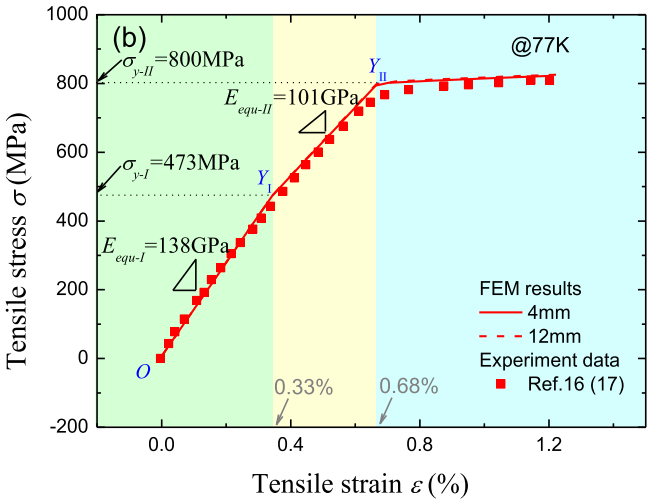

Figure 9. Comparison of tensile stress versus applied tensile strain between experimental data and simulated results on 4 mm and 12 mm REBCO conductors: (a) RT case, (b) 77 K case.

and analytical calculation results in [8], the FE modeling results in [11] and the multi-step simulations presented above. The multi-step method produces a residual strain that matches well with the experimental data at RT and closes to the analytical calculation in [8] and FE modeling result in [11] at 77 K.

Figure 8 shows the residual strain distributions due to thermal mismatch on all the constituent layers at RT and 77 K. For the same reasons stated above that explain the phenomena depicted in figure 6, the residual strain distributions on all the layers other than the silver layer, vary relatively in similar trends seen in the corresponding stress distributions shown in figure 6, while the tensile strains on the silver layer are larger than those on the copper layer at both RT and 77 K.

3.2. Uniaxial tensile load simulation

Uniaxial tensile tests generating stress–strain curves are the most common method for characterizing the mechanical properties of many materials, including composites. Here, a

longitudinal uniaxial tensile load is implemented within the conductor model with the thermal residual stresses and strains accumulated from the fabrication and cooling processes set as the initial stress and strain states. The stresses and strains at both the conductor and constituent-layer levels are studied.

3.2.1. Stress and strain analyses at the conductor level. Figure 9 shows the simulation results of the stress–strain relationship under tension for the REBCO conductor at RT and 77 K. Here the tensile strain ε and tensile stress σ are calculated as the engineering stress and engineering strain [16, 17] as:

$$\varepsilon = \frac{l - l_0}{l_0}, \tag{15}$$

$$\sigma = \frac{F}{A_0}, \tag{16}$$

where l_0 is the original length of the conductor and l is the final simulated length of the conductor, F is the applied tension load used in simulations and A_0 is the original cross-section area of the conductor. The mechanical parameters of the stabilizer and substrate and the data for validation are obtained from [16, 17]. The tested sample used in [16, 17] was a 12 mm wide REBCO conductor, however, simulations showed that a 4 mm wide conductor is sufficient for accurate simulation. As a result, the simulation results presented in this paper, including those in the previous section, are all based on a 4 mm wide conductor. To justify this decision, the stress–strain curves shown in figure 9 are generated from both the 4 mm conductor model and a 12 mm counterpart. The calculated stress–strain curves for the 4 and 12 mm are almost identical and agree well within the experimental data taken from [16, 17] on a 12 mm conductor.

When observed at the composite conductor level, the tensile stress computed by (16) can be estimated as the equivalent stress σ_{equ} of the composite based on the volume-weighted-average (13). Adding side copper stabilizer (20 μm thick each side) has little impact on the conductor-level equivalent stresses in the 4 and 12 mm conductors because the volumetric ratio of the side copper stabilizer to the other layers in either conductor is very small. Furthermore, the volumetric ratios of the surround copper stabilizer to the 4 mm and 12 mm conductors are 0.4348 and 0.4311, respectively, and the ratios of the Hastelloy layer to the conductors are 0.5312 and 0.5347, respectively. These small differences in the ratios between the 4 and 12 mm conductors are the reasons that the calculated conductor-level results from the 4 and 12 mm conductors are nearly identical. As a result, the 12 mm conductor experimental data taken from [16, 17] is used to validate the simulation results generated by the 4 mm conductor model. Conversely, the simulation results generated by the 4 mm conductor model can used to represent the mechanical behavior of a 12 mm conductor.

It is interesting to observe from figure 9 that as an elastic-plastic composite, the stress–strain curves of the REBCO conductors at RT and 77 K can be divided into three stages, represented by three different color zones, via two yield points Y_I and Y_{II}. As the copper stabilizer and Hastelloy substrate are the main components of the composite structure, the mechanical behavior of the REBCO conductor is mainly determined by these two layers. Using the materials properties listed in table 1, it can be deduced that the yield points Y_I and Y_{II} are due to the yielding of copper and Hastelloy, respectively. Specifically, from point O to Y_I, both the copper and Hastelloy layers are in the elastic stage; From Y_I to Y_{II}, copper yields but Hastelloy is still in the elastic stage. At Y_{II} and beyond, both copper and Hastelloy yield. Taking the RT case shown in figure 9(a) as an example, the equivalent elastic moduli (i.e. the slopes) of the first stage E_{equ-I} and the second stage E_{equ-II} are ~127 GPa and ~95 GPa, which are nearly equal to the volume-weighted-average Young's moduli at these stages. The volume-weighted-average Young's moduli are calculated by an equation similar to (13) but with the stress of each constituent layer replaced by its Young's (before yielding) or tangent (after yielding) modulus. The two yield stresses σ_{Y-I} and σ_{Y-II} found in figure 9(a), ~343 MPa and ~625 MPa respectively, are nearly the same as the volume-weighted-averages of the stresses (calculated from table 1) at points Y_I and Y_{II}. The corresponding tensile strains are found from the curves to be ~0.27% and 0.57%, respectively. Similarly, from the 77 K case shown in figure 9(b), the two equivalent elastic moduli, which are ~138 and ~101 GPa, and the corresponding yield stresses, which are ~473 and ~800 MPa, are also about the same as the corresponding volume-weighted-averages of Young's moduli and stress counterparts, with the corresponding tensile strains equal to ~0.33% and ~0.68%. Note that although all the layers in the conductor experience the same engineering tensile strain and the yields of the conductor at points Y_I and Y_{II} result from the yielding of the copper and Hastelloy layers, the conductor-level yield strains at Y_I and Y_{II} are in general different from the intrinsic yield strains of copper and Hastelloy. For example, the intrinsic yield strain of copper at 77 K as calculated from table 1 is 330 MPa/85 GPa =0.388%, while the yield strain at Y_I at 77 K is 0.33%, here 330 MPa and 85 GPa are respectively the yield stress and Young's modulus of copper. This discrepancy is due to the fact that the copper layer is pre-strained by the thermal residual strain (~0.068%, see figure 8) at 77 K before the tensile test.

3.2.2. Stress and strain analyses at the constituent layer level

3.2.2.1. Internal strain on the REBCO layer. The current-carrying capability of a REBCO conductor is dependent on the electromechanical properties and state of the REBCO layer, and in particular the strain in the REBCO layer. Figure 10 shows the dependence of the internal strain ε_{in}^{s} of the REBCO layer on the applied tensile strain ε at RT. Here ε_{in}^{s} is the internal strain induced by both thermal mismatch and tensile deformation. For a typical brittle material, a linear elastic constitutive relation is used to model mechanical properties until damage occurs. In this model, yield is used to represent the occurrence of damage in the brittle layers. As REBCO is a brittle material, elastic strain is needed to distinguish the undamaged, elastic behavior from the

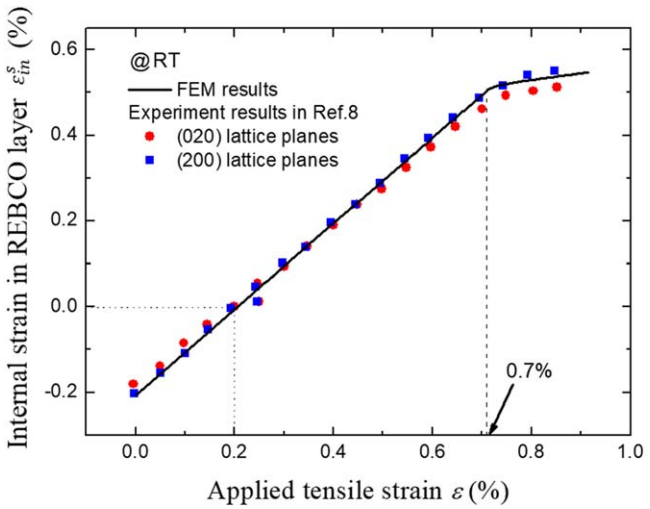

Figure 10. Comparison of internal strain versus applied tensile strain on the REBCO layer between experimental data and simulated results.

damaged one, however, an internal strain calculated by equation (14) contains both the elastic and plastic components. To distinguish the plastic strain, the internal strain is calculated directly as follow:

$$\varepsilon^s_{in} = \frac{1}{E^s}[\sigma^s_{xx} - \upsilon^s(\sigma^s_{yy} + \sigma^s_{zz})], \tag{17a}$$

where σ^s_{xx}, σ^s_{yy} and σ^s_{zz} are the principal stresses on the REBCO layer in the longitudinal, width and thickness directions, respectively, and E^s and υ^s are the Young's modulus and Poison's ratio of REBCO, respectively. As σ^s_{zz} is nearly zero, it can be simplified as,

$$\varepsilon^s_{in} = \frac{1}{E^s}[\sigma^s_{xx} - \upsilon^s\sigma^s_{yy}]. \tag{17b}$$

The elastic deformation behavior is seen in figure 10 from zero to 0.7% applied tensile strain. When ε is larger than 0.7%, the slope of ε^s_{in} reduces, signifying a yield accompanied with a damage, such as a crack on the REBCO layer, as mentioned in [8]. At zero applied external strain, a compressive residual strain of 0.20% generated during the fabrication process remains on the REBCO layer at RT, as seen in figure 8. When an external tensile load is applied, the compressive residual strain on the REBCO layer decreases and reaches zero at $\varepsilon = 0.20\%$, which is defined as the force-free strain in [8]. Beyond this strain, the internal strain of the REBCO layer changes into a tensile component with the increase of ε. Before yield, the strain curve is nearly linear, and the inclination angle of this curve is about 45°. The relationship between ε^s_{in} and ε satisfies,

$$\varepsilon^s_{in} = \varepsilon + \varepsilon^s_{res}, \tag{18}$$

where ε^s_{res} is the thermal residual strain in the REBCO layer in the longitudinal direction accumulated in the fabrication process from the initial fabrication temperature to RT. From figure 10, it can be seen that the simulation results agree well with the tested data taken from on the elastic part and yield

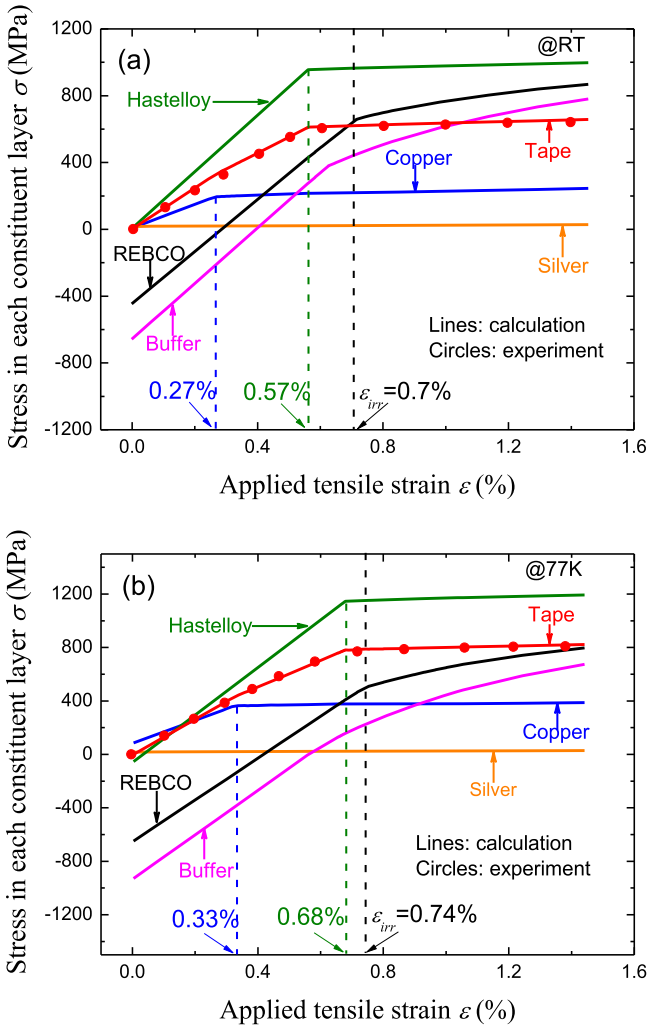

Figure 11. Stresses on all the constituent layers versus applied tensile load: (a) RT, (b) 77 K.

point. This indicates that using elastic and plastic yield properties together, the model can characterize well the deformation behavior and occurrence of relaxation (at yield point) on the brittle superconducting layer in REBCO conductors. According to [8], a relaxation was caused by damage, such as cracks. When a tensile load is applied to a REBCO coated conductor, the mechanical properties, such as the strain curve, can be separated into three stages: elastic, micro-yielding, and macro-yielding regions [35]. In the macro-yielding region, damage-like cracks are introduced, resulting in irreversible degeneration of I_c. In the model, an onset of such damage-induced relaxation on a brittle layer is identified as yielding. Note that the calculated smaller slope in ε^s_{in} after 0.7% is due to the yielded plastic stress components, however, since E^s is always used in (17) instead of E^s_t after fracture (represented by yielding in this model), (17) may not capture the after-yield internal strain accurately. The latter, however, is not important since for the REBCO layer, finding the yield point which represents the onset of damage is what matters most. The damaged part, i.e. the strain curve after yielding, has no physical meaning for a brittle material in the model and its slope is governed by the tangent modulus E^s_t,

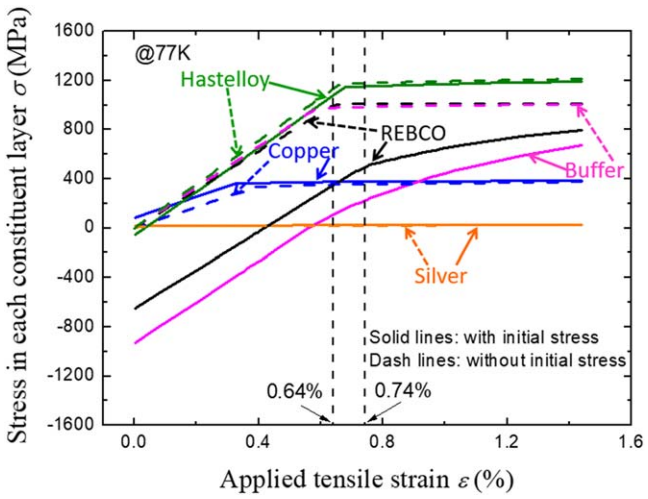

Figure 12. Comparison between the calculated stress–strain curves with (solid lines) and without (dashed lines) thermal-mismatch residual stresses and strains added.

which, for REBCO (and buffer), is much smaller than E^s (1 GPa versus 157 GPa). The small E_t^s of the brittle REBCO and buffer layers result in small plastic contributions, which, as mentioned in section 2.2, produce negligible effects on the overall stress and strain simulation results.

3.2.2.2. Stress distribution on all constitute layers. Figure 11 shows the stress on each constituent layer versus applied tensile strain ε at RT and 77 K. As seen in figure 5, due to thermal mismatch, there are non-zero residual stresses on all layers at zero applied tensile strain, including large compressive residual stresses accumulated on the REBCO and buffer layers.

The total residual stress of the composite conductor at zero applied tensile strain, however, is zero, as shown by the volume-weighted-average calculations based on (13) and data taken from figure 5 at both RT and 77 K in section 3.1.1. The compressive stresses on the REBCO and buffer layers first reduce to zero and then become tensile as the applied tensile load increases. When ε reaches ~0.7% at RT and ~0.74% at 77 K, the slope of the stress on the REBCO layer reduces due to yielding, signifying the onsets of damage and irreversible degradation in the critical current. This critical strain is the irreversible strain denoted as ε_{irr}. The value of ε_{irr} at 77 K (~0.74%) is in agreement with the experimental results presented in [8, 11, 16, 17, 40, 41]. The stress on the silver layer is nearly unchanged during the entire tensile test at both RT and 77 K because silver has already yielded in the fabrication process and it has a weak strain hardening with a small tangent modulus of 1 GPa. The stress–strain curves of copper and Hastelloy layers show the typical elastoplastic deformation properties. The applied tensile strains corresponding to the yield points of copper are 0.27% at RT and 0.33% at 77 K, which correspond to the first yield points in the stress–strain curves seen in figure 9. The applied strains for the yield points of Hastelloy are 0.57% at RT and 0.68% at 77 K, which correspond to the second yield points in the stress–strain curves seen in figure 9. The stress–strain curves for the 4 mm conductor and experimental data shown in figure 9 are repeated in figure 11 for comparison.

To study the effect of residual stresses and strains accumulated from the fabrication and cooling processes on the accuracy of mechanical analysis, the same uniaxial tensile test presented before is rerun on the same conductor model without the residual stresses and strains as the initial stresses and strains. The comparison between the calculated stress–strain curves is shown in figure 12 for 77 K. Note that on the model without initial residual stresses and strains added, all the stresses start from zero at zero applied tensile strain. Recall that there are non-zero residual stresses on all layers at zero applied tensile strain on the model with initial residual stresses and strains added, despite there is null total residual stress on the composite conductor. Although there are no big differences on the copper and Hastelloy layers in these two calculations, significant discrepancies appear on the REBCO and buffer layers. The calculation from the model with the residual stresses and strains considered, as shown in figure 11(b), shows that the tensile loading starts with large compressive stresses on the REBCO and buffer layers and results in $\varepsilon_{irr} = 0.74\%$ at 77 K. The calculation without the residual stresses and strains included, however, shows that the tensile loading starts with zero initial stresses on all layers and consequently results in a smaller $\varepsilon_{irr} = 0.64\%$. This comparison indicates that neglecting residual stresses and strains accumulated from thermal mismatch, and likely also from tension and bending, leads to unreliable simulation results. This is particularly important when considering the mechanical state of the REBCO layer and its relationship to the critical current.

As fractures such as cracks are more likely to be caused by tensile strain than by compressive strain, the results in figure 12 imply that the mechanical integrity and the current-carrying capability of the REBCO layer are enhanced by compressive residual stresses and strains generated in the fabrication and cooling processes. It is plausible that compressive residual stresses and strains would also affect the results for cyclic fatigue measurements. Since the stresses induced by thermal mismatch are in-plane for the thin film layers, with negligible component in the thickness direction, the same compressive residual stress and strain are generated in both the longitudinal and width directions on the REBCO layer during the fabrication and cooling processes. When a longitudinal uniaxial tensile load is applied to the conductor, however, the compressive residual strain on the REBCO layer in the longitudinal direction is released and the compressive strain in the width direction is increased. The von-Mises yield criterion in the principal plane stress state, which can be simplified as $\sigma_V = \sqrt{\sigma_{xx}^2 - \sigma_{xx}\sigma_{yy} + \sigma_{yy}^2}$, is commonly used to determine the onset of yielding in a ductile material. In the conductor model, this yield criterion is also used to determine the onset of damage on the REBCO layer. This implies that the critical yield strain ε_{irr} is not only related to the stress state in the longitudinal direction but also the stress state in the width direction of the REBCO layer. This indicates that a 3D structural model similar to the model presented here is

necessary to obtain accurate stress and strain information for complex composites like REBCO conductors. Note that because the von-Mises yield criterion uses REBCO's yield strength $\sigma_y = 1030$ MPa to determines the onset of yielding on the REBCO layer, the longitudinal yield stress of REBCO layer with ~650 MPa at 77 K and at ~500 MPa at RT, as seen in figure 11, is smaller than σ_y.

3.3. Critical current under uniaxial tension

The strain effect on I_c can be divided into two regions: reversible and irreversible. The Ekin power-law formula [29] has been used to predict the reversible degradation of I_c under uniaxial strain in REBCO conductors [8, 12]. Irreversible degradation of I_c is caused by damage on the REBCO layer [17–19]. Furthermore, irreversible degradation of I_c in both BSCCO-based (e.g. Bi-2212 and Bi-2223) and REBCO conductors has been studied using a statistical approach based upon the Weibull statistics [31, 32, 42–45]. Here a critical current phenomenological model that combines the Ekin power-law formula and the Weibull distribution function with the REBCO conductor model is used to predict the electro-mechanical behavior of I_c in REBCO conductors across the entire strain range.

Suppose ε is the strain within a REBCO conductor from a uniaxial loading, the applied strain dependence of the critical current density j_ε normalized by the maximum critical current density $j_{\max}$ in the reversible region is formulated by Ekin's power-law formula is [29]:

$$\frac{j_\varepsilon}{j_{\max}} = 1 - a\,|\varepsilon - \varepsilon_{\max}|^b, \tag{19}$$

where $\varepsilon_{\max}$ is the so-called maximum strain, at which the critical current density reaches the maximum value $j_{\max}$, a and b are constants, which are determined by curve fitting on the experimental data taken from the reversible part. Using equation (19), the reversible strain dependence of critical current density normalized by the current density under zero-strain j_{c0} can be written as:

$$\frac{j_\varepsilon}{j_{c0}} = \frac{1}{1 - a\,|\varepsilon_{\max}|^b}(1 - a\,|\varepsilon - \varepsilon_{\max}|^b). \tag{20}$$

Experimental results showed that irreversible degradation of I_c increased with the enlargement of crack propagation on the REBCO layer [17–19], indicating that the current-carrying capability was related to the effective undamaged cross-section area on the REBCO layer. Therefore, the strain-dependent critical current I_ε and zero-strain critical current I_{c0} can be calculated as:

$$I_\varepsilon = \int_{S_{eff}} j_\varepsilon dS, \quad I_{c0} = \int_{S_0} j_0 dS, \tag{21}$$

where S_{eff} is the effective undamaged cross-section area on the REBCO layer under uniaxial deformation, and S_0 denotes the cross-section area of the REBCO layer at the initial state with zero-strain.

Ignoring the linear deformation effect on the REBCO cross-section area, and assuming a uniform distribution of current on the REBCO layer, the normalized critical current I_ε/I_{c0} is obtained by:

$$\frac{I_\varepsilon}{I_{c0}} = \frac{j_\varepsilon}{j_{c0}}\frac{S_{eff}}{S_0}. \tag{22}$$

A statistical approach based upon the Weibull distribution function has been used to characterize the effective area of undamaged superconducting region under deformation in BSCCO-based conductors [42–45], and the irreversible degradation of I_c in both BSCCO-based and REBCO conductors [31, 32]. The statistical ratio of undamaged superconducting cross-section area to the before-damaged superconducting cross-section area under uniaxial loadings, S_{eff}/S_0, can be expressed using the Weibull distribution as:

$$\frac{S_{eff}}{S_0} = W(\varepsilon) = \begin{cases} 1 & if\ \varepsilon \leqslant \varepsilon_{irr} \\ \exp\left[-\left(\dfrac{\varepsilon - \varepsilon_{irr}}{\varepsilon_0}\right)^m\right] & if\ \varepsilon > \varepsilon_{irr} \end{cases}, \tag{23}$$

here the irreversible strain ε_{irr} under uniaxial tension load is determined from simulation, as demonstrated in the previous section, at the onset of damage occurs on the REBCO layer, i.e. when the REBCO layer yields. The parameters m and ε_0 are respectively the shape and scaling parameters of the Weibull function, which can be determined by curve fitting on experimental data taken from the irreversible part.

Combining (20)–(23) the applied strain-dependent normalized critical current model is written as:

$$\frac{I_\varepsilon}{I_{c0}} = \frac{1}{1 - a\,|\varepsilon_{\max}|^b}(1 - a\,|\varepsilon - \varepsilon_{\max}|^b)\,W(\varepsilon). \tag{24a}$$

Using (23), the model is rewritten as:

$$\frac{I_\varepsilon}{I_{c0}} = \begin{cases} \dfrac{1}{1 - a\,|\varepsilon_{\max}|^b}(1 - a\,|\varepsilon - \varepsilon_{\max}|^b) & if\ \ \varepsilon \leqslant \varepsilon_{irr} \\ \dfrac{1}{1 - a\,|\varepsilon_{\max}|^b}(1 - a\,|\varepsilon - \varepsilon_{\max}|^b)\exp\left[-\left(\dfrac{\varepsilon - \varepsilon_{irr}}{\varepsilon_0}\right)^m\right] & if\ \ \varepsilon > \varepsilon_{irr} \end{cases}. \tag{24b}$$

Using the critical current model above, the critical current dependence on the tensile strain can be investigated. The terms in (24*b*) for the $\varepsilon_{irr} \leqslant \varepsilon_{irr}$ and $\varepsilon_{irr} > \varepsilon_{irr}$ cases represent the reversible change and irreversible degradation of I_c,

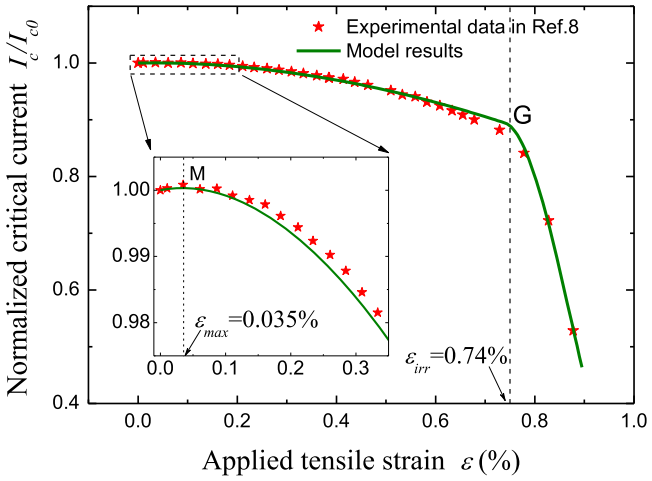

Figure 13. Comparison between simulation results and experimental data for the strain dependence of normalized critical current.

respectively. The parameters in the reversible term of equation (24*b*) are adopted from [8] as $a = 1300$, $b = 1.9$ and $\varepsilon_{max} = 0.035\%$. Based on the simulation results in figure 11, the irreversible strain $\varepsilon_{irr} = 0.74\%$ is used. The parameters $m = 2$ and $\varepsilon_0 = 0.21\%$ are found by curve fitting on the experimental data taken from the irreversible part in [8].

Figure 13 compares the simulation result calculated by (24) against the experimental data taken from [8] for the applied strain dependence of (normalized) critical current. The inset shows that I_c increases slightly to a maximum value at point M when the applied tensile strain increases from zero to $\varepsilon_{\max} = 0.035\%$. After reaching the peak, I_c decreases gradually and then drops sharply when the applied strain passes the point G, which is at the irreversible strain ε_{irr}. According to the experimental data in [8, 16, 17], the gradual degradation in I_c from zero strain to ε_{irr} is reversible and beyond ε_{irr}, irreversible degradation in I_c occurs due to damage of the REBCO layer. Figure 13 shows that the prediction from the model is in good agreement with the experiment data in both the reversible and irreversible degradation regions.

4. Conclusion

An elastoplastic FE model HAR laminated composite model is constructed for stress and strain analyses of REBCO conductors during fabrication and cooling and under tensile load. The 3D/2D mixed-dimensional modeling method is used to overcome the meshing and computation difficulties commonly encountered in modeling laminated thin-film multilayers in full-3D FE models. This approach allows all major constituent layers of a conductor to be included and modeled in real dimensions independent of the thicknesses of the individual layers.

Results show that the multi-step modeling method for fabrication of a conductor is an essential and effective method for residual stress and strain analyses in REBCO conductors during fabrication and cooling. Non-zero thermal residual stresses accumulated during fabrication and cooling exist on all the constituent layers. In particular, compressive thermal residual stress generated on the REBCO layer strongly affects the mechanical properties of the REBCO layer under tension load. Tensile loading simulation shows that the stress–strain curves of REBCO conductor at RT and 77 K can be divided into three stages separated by two yield points, one due to the yield of copper and the other due to the yield of Hastelloy. The irreversible strain where the onset of damage occurs on the REBCO layer is found to be about 0.7% at RT and 0.74% at 77 K. The stress and strain distributions under applied load at both the conductor level and constituent-layer level are experimentally validated. Simulation results show that the critical current model based on the Ekin power-law formula and Weibull distribution function can predict the I_c versus strain electromechanical behavior of REBCO conductor in both the reversible and irreversible degradation regions.

Acknowledgments

Peifeng Gao would like to acknowledge the supports by the National Natural Science Foundation of China (11902129, 11932008, 11672120), the China Postdoctoral Science Foundation (2019T120963, 2018M633604), Initial Scientific Research Fund of Lanzhou University for Young Researcher Fellow and the Fundamental Research Funds for the Central Universities (lzujbky-2018-it01, lzujbky-2018-it27). Peifeng Gao would like to thank Chunlin Pan and Yujin Tong for their helpful discussions and suggestions.

Appendix. Stress distribution in the width direction

For a real REBCO conductor, the edges are usually composed of electroplated copper or solder fillet. In such a structure, the side material creates boundary constraints on the outer sides of each constituent layer, and so the outer side boundaries of each constituent layer are no longer free. As a result, inhomogeneous stress distributions appear on all the constituent layers along the regions near the edges. Figure A1 shows the residual stress distributions of all the constituent layers of a half-width (2 mm) conductor in the width direction at 77 K. The stress distribution on each layer is nearly homogeneous in the width direction from the center to 1.9 mm, while inhomogeneous stress distributions appear near the edge from 1.9 to 2 mm. The homogeneous stress distribution region takes up about 95% of the width and the mechanical and superconducting properties are mainly determined by the performance of this region. As a result, the stresses on all the constituent layers are obtained from their longitudinal centers, which are within the homogeneous stress distribution region. In addition, it can also be seen that the stresses on the top and bottom copper layers are almost the same when measured at their half-thickness centers. Though the conductor structure in the thickness direction is not symmetrical, the thicknesses of the HAR laminated layers are so thin that their effects on the stress distributions of the copper layers are very small. Thus,

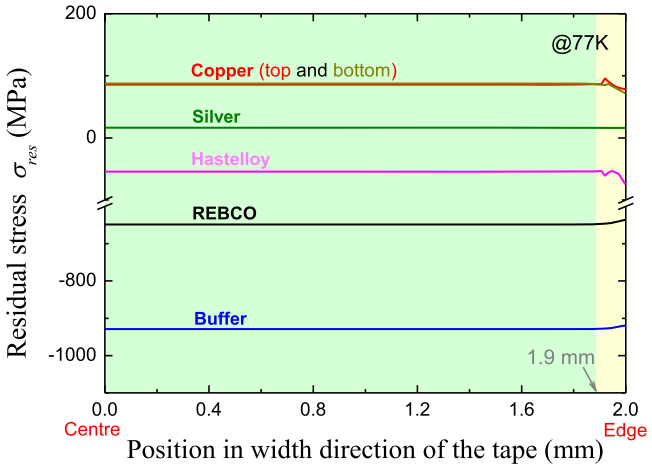

Figure A1. Residual stress distributions on all the constituent layers of a half-width conductor in the width direction at 77 K.

only the stress and strain information on the top copper layer is used in this paper.

ORCID iDs

Peifeng Gao https://orcid.org/0000-0002-2671-4955
Xingzhe Wang https://orcid.org/0000-0002-0537-4656

References

[1] Takayasu M, Chiesa L, Bromberg L and Minervini J V 2011 HTS twisted stacked-tape cable conductor *Supercond. Sci. Technol.* **25** 014011
[2] Goldacker W, Grilli F, Pardo E, Kario A, Schlachter S I and Vojenčiak M 2014 Roebel cables from REBCO coated conductors: a one-century-old concept for the superconductivity of the future *Supercond. Sci. Technol.* **27** 093001
[3] Ta W and Gao Y 2018 Numerical simulation of the electro-thermo-mechanical behaviors of a high-temperature superconducting cable *Compos. Struct.* **192** 616–25
[4] Hahn S *et al* 2019 45.5-tesla direct-current magnetic field generated with a high-temperature superconducting magnet *Nature* **570** 496–9
[5] Wang Y, Zhang M, Grilli F, Zhu Z and Yuan W 2019 Study of the magnetization loss of (RE)$Ba_2Cu_3O_x$ conductor on round core cable using 3D T-A formulation *Supercond. Sci. Technol.* **32** 025003
[6] Geng J and Coombs T 2015 Mechanism of a high-Tc superconducting flux pump: using alternating magnetic field to trigger flux flow *Appl. Phys. Lett.* **107** 142601
[7] Senatore C, Alessandrini M, Lucarelli A, Tediosi R, Uglietti D and Iwasa Y 2014 Progresses and challenges in the development of high-field solenoidal magnets based on RE123 coated conductors *Supercond. Sci. Technol.* **27** 103001
[8] Osamura K, Sugano M, Machiya S, Adachi H, Ochiai S and Sato M 2009 Internal residual strain and critical current maximum of a surrounded Cu stabilized YBCO coated conductor *Supercond. Sci. Technol.* **22** 065001
[9] Osamura K, Machiya S and Hampshire D P 2016 Mechanism for the uniaxial strain dependence of the critical current in practical REBCO tapes *Supercond. Sci. Technol.* **29** 065019
[10] Dizon J R C, Nisay A R N, Dedicatoria M J A, Munoz R C, Shin H-S and Oh S-S 2014 Analysis of thermal residual stress/strain in REBCO coated conductor tapes *IEEE Trans. Appl. Supercond.* **24** 1–5
[11] Ilin K, Yagotintsev K, Zhou C, Gao P, Kosse J, Otten S, Wessel W A, Haugan T, van der Laan D and Nijhuis A 2015 Experiments and FE modeling of stress–strain state in ReBCO tape under tensile, torsional and transverse load *Supercond. Sci. Technol.* **28** 055006
[12] van der Laan D C, Haugan T J and Barnes P N 2009 Effect of a compressive uniaxial strain on the critical current density of grain boundaries in superconducting $YBa_2Cu_3O_{7-\delta}$ films *Phys. Rev. Lett.* **103** 027005
[13] Gao P, Zhang R and Wang X 2017 Pressure induced self-doping and dependence of critical temperature in stoichiometry $YBa_2Cu_3O_{6.95}$ predicted by first-principle and BVS calculations *AIP Adv.* **7** 035215
[14] Osamura K, Machiya S, Kajiwara K, Kawasaki T, Harjo S, Zhang Y, Fujita S, Iijima Y and Hampshire D 2019 Inverted-parabolic and weak strain dependencies on the critical current in practical ⟨110⟩ and ⟨100⟩ oriented REBCO tapes *AIP Adv.* **9** 075216
[15] Shin H S and Bautista Z 2019 Establishing a test procedure for evaluating the electromechanical properties of practical REBCO coated conductor tapes by the uniaxial tension test at 77 K *Supercond. Sci. Technol.* **32** 064004
[16] Zhang Y 2014 Mechanical and electromechanical properties of IBAD-MOCVD-based REBCO coated conductors *Int. Workshop on Coated Conductors for Applications (Jeju, South Korea)*
[17] Zhang Y, Hazelton D, Kelley R, Kasahara M, Nakasaki R, Sakamoto H and Polyanskii A 2016 Stress–strain relationship, critical strain (stress) and irreversible strain (stress) of IBAD-MOCVD-based 2G HTS wires under uniaxial tension *IEEE Trans. Appl. Supercond.* **26** 1–6
[18] Sugano M, Osamura K, Prusseit W, Semerad R, Itoh K and Kiyoshi T 2005 Tensile fracture behaviour of RE-123 coated conductors induced by discontinuous yielding in Hastelloy C-276 substrate *Supercond. Sci. Technol.* **18** S344
[19] Rogers S, Chan W K and Schwartz J 2016 Effects of room-temperature tensile fatigue on critical current and n-value of IBAD–MOCVD $YBa_2Cu_3O_{7-x}$/Hastelloy coated conductor *Supercond. Sci. Technol.* **29** 085013
[20] Ta W, Liu Y, Wang K, Liu L and Gao Y 2018 Effect of the twisting chirality configuration on the electromechanical behavior of multilayer superconducting tapes *Phys. Lett.* A **383** 949–56
[21] Dizon J R C, Gorospe A B and Shin H-S 2014 Numerical analysis of stress distribution in Cu-stabilized GdBCO CC tapes during anvil tests for the evaluation of transverse delamination strength *Supercond. Sci. Technol.* **27** 055023
[22] Liu W, Zhang X, Zhou J and Zhou Y 2015 Delamination strength of the soldered joint in YBCO coated conductors and its enhancement *IEEE Trans. Appl. Supercond.* **25** 6606109
[23] Liu L, Zhu Y, Yang X, Qiu T and Zhao Y 2016 Delamination properties of YBCO tapes under shear stress along the width direction *IEEE Trans. Appl. Supercond.* **26** 1–6
[24] Celik E, Sayman O, Karakuzu R and Ozman Y 2007 Numerical analysis of the influence of buffer layer thickness on the residual stresses in YBCO/$La_2Zr_2O_7$/Ni superconducting materials *Mater. Des.* **28** 2184–9
[25] Hsueh C and Paranthaman M 2008 Analytical modeling of residual stresses in multilayered superconductor systems *J. Mater. Sci.* **43** 6223–32

[26] Chan W K, Masson P J, Luongo C and Schwartz J 2010 Three-dimensional micrometer-scale modeling of quenching in high-aspect-ratio $YBa_2Cu_3O_{7-\delta}$ coated conductor tapes: I. Model development and validation *IEEE Trans. Appl. Supercond.* **20** 2370–80

[27] Chan W K and Schwartz J 2011 Three-dimensional micrometer-scale modeling of quenching in high-aspect-ratio $YBa_2Cu_3O_{7-\delta}$ coated conductor tapes :II. influence of geometric and material properties and implications for conductor engineering and magnet design *IEEE Trans. Appl. Supercond.* **21** 3628

[28] Gao P, Chan W-K, Wang X and Schwartz J 2018 Mixed-dimensional modeling of delamination in rare earth-barium-copper-oxide coated conductors composed of laminated high-aspect-ratio thin films *Supercond. Sci. Technol.* **31** 074004

[29] Ekin J W 1984 Strain effects in superconducting compounds *Adv. Cryog. Eng.* **30** 823–36

[30] Weibull W and Sweden S 1951 A statistical distribution function of wide applicability *J. Appl. Mech.* **18** 293

[31] Mbaruku A, Le Q, Song H and Schwartz J 2010 Weibull analysis of the electromechanical behavior of AgMg sheathed $Bi_2Sr_2CaCu_2O_{8+x}$ round wires and $YBa_2Cu_3O_{7-\delta}$ coated conductors *Supercond. Sci. Technol.* **23** 115014

[32] Oh S-S, Kim H-S, Ha D-W, Ha H-S, Sim K, Dizon J R C and Shin H-S 2014 Variation of local critical current due to mechanical strain in RCE-REBCO coated conductors *IEEE Trans. Appl. Supercond.* **24** 6900204

[33] Hazelton D W 2011 2G HTS Applications Developments *Symposium on Superconducting Devices for Wind Energy (Barcelona, Spain)*

[34] Boresi A P, Schmidt R J and Sidebottom O M 1985 *Advanced Mechanics of Materials* vol 6 (New York: Wiley)

[35] Osamura K, Sugano M, Machiya S, Adachi H, Sato M, Ochiai S and Otto A 2007 Reversibility of micro-yielding and critical current in a YBCO-coated conductor caused by a uniaxial tensile load *Supercond. Sci. Technol.* **20** S211–6

[36] Ochiai S, Rokkaku H, Morishita K, Shin J, Iwamoto S, Okuda H, Hojo M, Osamura K, Sato M and Otto A 2007 Thermally induced residual strain accumulation in Bi2223/Ag/Ag alloy composite superconductor *Supercond. Sci. Technol.* **20** 202

[37] Zhang Z, Chen W and Gou X 2014 Numerical studies of thermally induced residual strain/stress in $Bi_2Sr_2Ca_2Cu_3O_x$/Ag/Ag alloy composite tapes and the dependence of material properties on the temperature *J. Supercond. Novel Magn.* **27** 1387–96

[38] Cheon J, Shankar P and Singh J 2004 Influence of processing methods on residual stress evolution in coated conductors *Supercond. Sci. Technol.* **18** 142

[39] Mori M, Watanabe T, Kashima N, Nagaya S, Muroga T, Miyata S, Yamada Y, Izumi T and Shiohara Y 2006 Development of long YBCO coated conductors by multiple-stage CVD *Physica* C **445** 515–20

[40] Shin H-S and Dedicatoria M J 2013 Intrinsic strain effect on critical current in Cu-stabilized GdBCO coated conductor tapes with different substrates *Supercond. Sci. Technol.* **26** 055005

[41] Barth C, Mondonico G and Senatore C 2015 Electro-mechanical properties of REBCO coated conductors from various industrial manufacturers at 77 K, self-field and 4.2 K, 19 T *Supercond. Sci. Technol.* **28** 045011

[42] Gao P and Wang X 2014 Critical-current degeneration dependence on axial strain of bi-based superconducting multi-filamentary composite tapes *Chin. Phys. Lett.* **31** 047401

[43] Gao P, Xin C, Guan M, Wang X and Zhou Y 2016 Strain effect on critical current degradation in Bi-based superconducting tapes with different deformation modes *IEEE Trans. Appl. Supercond.* **26** 1–5

[44] Gao P and Wang X 2018 Analysis of torsional deformation-induced degeneration of critical current of Bi-2223 HTS composite tapes *Int. J. Mech. Sci.* **141** 401–7

[45] Gao P, Wang X and Zhou Y-H 2019 Strain dependence of critical current and self-field AC loss in Bi-2223/Ag multi-filamentary HTS tapes: a general predictive model *Supercond. Sci. Technol.* **32** 034003